Corrosion Science 225 (2023) 111569

Contents lists available at ScienceDirect

Corrosion Science

journal homepage: www.elsevier.com/locate/corsci

Unravelling the effect of F phase on hydrogen-assisted intergranular cracking in nickel-based Alloy 725: Experimental and DFT study

Xu Lu [a,*], Yan Ma [b,**], Yuan Ma [c,**], Dong Wang [a], Lei Gao [c], Wenwen Song [d], Lijie Qiao [c], Roy Johnsen [a]

[a] Department of Mechanical and Industrial Engineering, Norwegian University of Science and Technology, Richard Birkelands vei 2B, N-7491 Trondheim, Norway
[b] Max-Planck-Institut für Eisenforschung, 40237 Düsseldorf, Germany
[c] Beijing Advanced Innovation Center for Materials Genome Engineering, University of Science and Technology Beijing, 100083 Beijing, China
[d] Granularity of Structural Information in Materials Engineering, Institute of Materials Engineering (ifW), University of Kassel, Moenchebergstr. 3, 34125 Kassel, Germany

ARTICLE INFO

Keywords:
Nickel Alloy 725
Hydrogen embrittlement
F phase
Grain boundary
Density functional theory

ABSTRACT

The effect of the scarcely reported F phase on hydrogen-assisted cracking in nickel-based Alloy 725 was thoroughly studied by combining tensile tests, advanced characterization, and density functional theory (DFT) calculations. The results show grain boundary precipitate F phase promotes intergranular fracture in a hydrogen environment. DFT calculations further indicates hydrogen atoms lower the binding strength of the F phase and Ni matrix interfaces. More importantly, our study showed for the first time that the addition of approximately 0.01 wt.% boron can effectively suppress F phase precipitation, thereby elevating the hydrogen resistance of Alloy 725.

1. Introduction

Because global energy demands still rely on oil and gas exploitation, the performance of the equipment components in this field has continuously attracted attention. Nickel-based alloys, particularly precipitation-hardened alloys, are extensively used owing to their combination of excellent mechanical properties, good corrosion resistance, and wide working temperature range (up to 1200 °C) [1]. By designing proper heat treatments and doping with Cr and other refractory elements (e.g., Mo, W, and Re), high corrosion resistance and effective solid solution strengthening can be obtained via the homogeneous dispersion of two strengthening phases, that is, gamma prime (γ', Ni_3Al/Ti, $L1_2$, cubic, $Pm\bar{3}m$) and gamma double prime (γ'', Ni_3Nb, $D0_{22}$, tetragonal, $I4/mmm$) [1,2]. In addition, other phases can form in the matrix or along the grain boundary (GB), such as carbides, carbonitrides, δ phase (Ni_3Nb, $D0_a$, orthorhombic, P/mmn) [3], η phase ($Ni_3Nb_{0.5}(Al/Ti)_{0.5}$, $D0_{24}$, hexagonal, $P6_3/mmc$), and σ phase (tetragonal, $P4_2/mnm$) [2]. The existence of the latter phases deteriorates the mechanical properties, particularly, when hydrogen is present in the environment [3–6]. The hydrogen-induced premature failure of a structural component is called hydrogen embrittlement, and it is considered a crucial challenge for the application of these alloys in the oil and gas industries [7]. Thus, safety regulations have driven research efforts to understand the fundamental hydrogen embrittlement mechanisms and design hydrogen-tolerant alloys.

The exploration of hydrogen-induced fractures in nickel alloys can be traced back several decades [8]. Both hydrogen-induced transgranular and intergranular fractures have been observed [9–16]. Transgranular cracking is often linked to microvoid formation at dislocation slip band intersections [9]. However, the mechanism of hydrogen-induced intergranular cracking is not fully elucidated because of the complex microstructural features at the GBs. Density functional theory (DFT)-based simulations showed a high impact of the GB internal structure on hydrogen trapping and diffusion behavior [17]. The co-segregation of hydrogen and other alloying elements has either a strengthening (e.g., H-Mo) or weakening (e.g., H-C) effect on the susceptibility of GB decohesion [18]. In addition, experimental studies have linked hydrogen-assisted intergranular fractures with GB secondary phases such as δ phase, σ phase, and carbide/carbonitride. Most recent

* Correspondence to: Department of Mechanical and Industrial Engineering (MTP), Norwegian University of Science and Technology (NTNU), Richard Birkelandsvei 2B, NO-7491 Trondheim, Norway.
** Corresponding authors.
E-mail addresses: xu.lu@ntnu.no (X. Lu), y.ma@mpie.de (Y. Ma), yuanma@ustb.edu.cn (Y. Ma).

https://doi.org/10.1016/j.corsci.2023.111569
Received 30 March 2023; Received in revised form 21 August 2023; Accepted 1 October 2023
Available online 4 October 2023

findings have demonstrated that the intergranular δ phase assists in crack initiation and provides a pathway for crack propagation [3,5,10,19]. Both transgranular cleavage and intergranular cracks that originated from the δ phase have been frequently reported [5,10]. The mechanism was claimed to be the reduction of the bonding strength at δ/matrix interfaces with hydrogen according to the "Defactant" concept [20–22]. In addition, microcracks can readily nucleate during plastic deformation because of their higher hydrogen adsorption capacity at these interfaces than in the matrix [6]. Moreover, the precipitation-free zone around the δ phase can effectively enhance strain localization and promote intergranular cracking [10]. Carbides/carbonitrides are another frequently discussed topic. Depending on the location of the carbide/carbonitride precipitates, different cracking behaviors were observed. GB carbide has been reported to trap hydrogen and contribute to a reduction in the GB cohesive energy. As a result, susceptibility to intergranular rupture is elevated [23,24]. In contrast, coarsened carbides/carbonitrides in the matrix trapped less hydrogen at the incoherent interfaces; thus, hydrogen-induced fractures occurred inside the carbide/carbonitride rather than at the interface [5,6,11,25].

Although tremendous efforts have been dedicated to unraveling the σ/δ/carbides-related hydrogen embrittlement in nickel alloys, the role of the GB F phase, a σ-related topologically close-packed (TCP) phase, in hydrogen-induced intergranular fracture remains unexplored. The F phase was first discovered in nickel alloys by Kuo and Steeds in 1986 [26,27], demonstrating that it is composed of hexagonal antiprisms and is rich in Mo and Cr. This phase formed the focus with regard to nickel-based Alloy 725 in the recent study by Hazarabedian et al. [28]. In practice, the F phase is not expected to be observed, as indicated by the time-temperature-transformation diagram in a previous study [29]. The crystallographic structure of the F phase can be erroneously judged and confused with that of the σ phase because they have similarities in both microstructural appearance and chemical composition. The F phase has been reported to exhibit hexagonal antiprisms and holds a similar projection to that of the [001] σ phase in the [0001] axis. Similar to the σ phase, internal faults form in the hexagonal F phase, the formation of which could also be ascribed to a complex synchro-shear mechanism on the (0001) basal plane [2,30]. Because of the small size of this phase, the determination of the crystalline structure typically requires advanced characterization techniques. Studies on the effect of the F phase in nickel alloys are scarce, not to mention those on the synergistic effect of hydrogen and the F phase. Thus, it is of paramount importance to precisely identify this phase and evaluate its interfacial properties with GBs in a hydrogen environment before further application. Considering the aforementioned factors, in this study, a substantial effort was made to investigate the hydrogen-induced fracture behavior at the F-phase-decorated GBs in modification no.1 (M1) nickel-based Alloy 725 using the current state-of-the-art experimental and simulation approaches, that is, meso-scale tensile testing, atom probe tomography (APT), and high-resolution transmission electron microscopy (TEM) in combination with DFT calculations. In addition, by doping the material with minor alloying elements boron (B) and copper (Cu), modified sample no.2 (M2), which is free from the F phase, was obtained. A comparison of the hydrogen embrittlement sensitivity of these two alloys was carried out. This study aimed to provide a comprehensive understanding of the crucial but rarely reported effect of the F phase on the hydrogen-interplayed straining process. In addition, an effective mitigation approach to eliminate the F phase precipitation by GB elemental partitioning was proposed in the framework of alloy design, with particular applicability in future GB segregation engineering in nickel alloys.

2. Methodology

2.1. Materials and experimental procedure

In this study, two modifications (M1 and M2) of Ni-based Alloy 725 were tested. M1 had a chemical composition similar to that of the commercial UNS N07725. M2 was slightly modified by the addition of B (~0.01 wt.%) and Cu (~2.1 wt%). The laboratory-melt Alloy 725 samples were produced by vacuum induction melting and then forged into a round bar with a diameter of 130 mm. The bars were solution-annealed at 1038 °C for 2 h and water-quenched, followed by two-step aging at 732 °C and 621 °C for 8 h, then, cooled in air to room temperature (~23 °C).

To determine the crystal structure of the F phase at the GB and its orientation relationship with the matrix, TEM (JEOL JEM ARM 200 F) and scanning transmission electron microscopy (STEM) analyses were applied to the lamellae samples at an operation voltage of 200 kV. Selected area diffraction (SAD) patterns were recorded to determine the lattice constants of the matrix. Nano-beam diffraction (NBD) was used to acquire the diffraction patterns of the F phase, considering its small size. The high-angle annular dark field (HAADF) imaging mode of STEM was applied to reveal the coherency between the F phase and nickel matrix. The chemical composition of the F phase was measured using both APT and energy dispersive X-ray spectroscopy (EDS) equipped in the TEM. APT measurements were conducted using a LEAP 4000X HR instrument in laser-pulsing mode at 60 K. The pulse frequency and laser energy were 250 kHz and 30 pJ, respectively. APT data were reconstructed using Integrated Visualization and Analysis Software package (IVAS 3.8.0, CAMECA Scientific Instruments, Madison, WI, USA). The elemental segregation behavior of precipitate-free GB in the M2 sample was investigated using another STEM (Hitachi High-Tech) in combination with EDS.

The effects of hydrogen on the mechanical properties of both the hydrogen-free and hydrogen-charged samples were investigated using uniaxial tensile testing. The gauge dimensions of the sample for tensile tests were 5 × 1 × 0.5 (length × width × thickness, in mm); more details can be found in Refs. [11,25]. The samples were prepared by grinding and polishing up to a 1 μm diamond paste. Electropolishing was performed in a methanolic H_2SO_4 solution at 26 V for 30 s as the final step to remove the deformation layer induced by mechanical polishing. Hydrogen pre-charging was completed in a mixture of glycerol and H_3PO_4 at a fixed current density of 15 mA/cm^2 for 18 h at 75 °C (348.15 K). After hydrogen charging, the sample was taken out from the electrolyte and rinsed with distilled water. During the rinse step, the sample was cooled to room temperature. The dwell time between the completion of hydrogen charging and start testing was approximately 20 min.

To characterize hydrogen profile after charging and before tensile testing caused by hydrogen degassing, hydrogen diffusivity should be acquired. An electrochemical permeation test was performed on a commercial Alloy 725 at room temperature (23 °C), which has a similar chemical composition and microstructure with the studied alloy. The permeation curve is shown in Fig. 1(a). Detailed information of the permeation setup was described in previous studies by the authors [31]. Hydrogen diffusivity calculated from Fig. 1(a) using time-lag method is 1.61 × 10^{-15} m^2/s at room temperature (23 °C). According to previous studies where diffusion equations were reported for nickel alloys [31,32], hydrogen diffusivity at 75 °C is about 20 times of that at room temperature. Therefore, it can be deduced that hydrogen diffusivity at current charging condition (75 °C) is 3.22 × 10^{-14} m^2/s (equals to 115.92 μm^2/hr), this value is comparable to the one obtained from Inconel 718 (2.53 × 10^{-14} m^2/s) in Ref. [32]. Hydrogen profile after hydrogen charging can be fitted using a non-steady state diffusion model [33]:

$$\&C(x,t) = C_1 + (C_2 - C_1)\frac{x}{l} + \frac{2}{\pi}\sum_{1}^{\infty}\frac{C_2\cos n\pi - C_1}{n}\sin\frac{n\pi x}{l}\exp\left(-\frac{Dn^2\pi^2 t}{l^2}\right) + \frac{2}{l}\sum_{1}^{\infty}\sin\frac{n\pi x}{l}\exp\left(-\frac{Dn^2\pi^2 t}{l^2}\right)\int_0^l f(x')\sin\frac{n\pi x'}{l}dx'\# \quad (1)$$

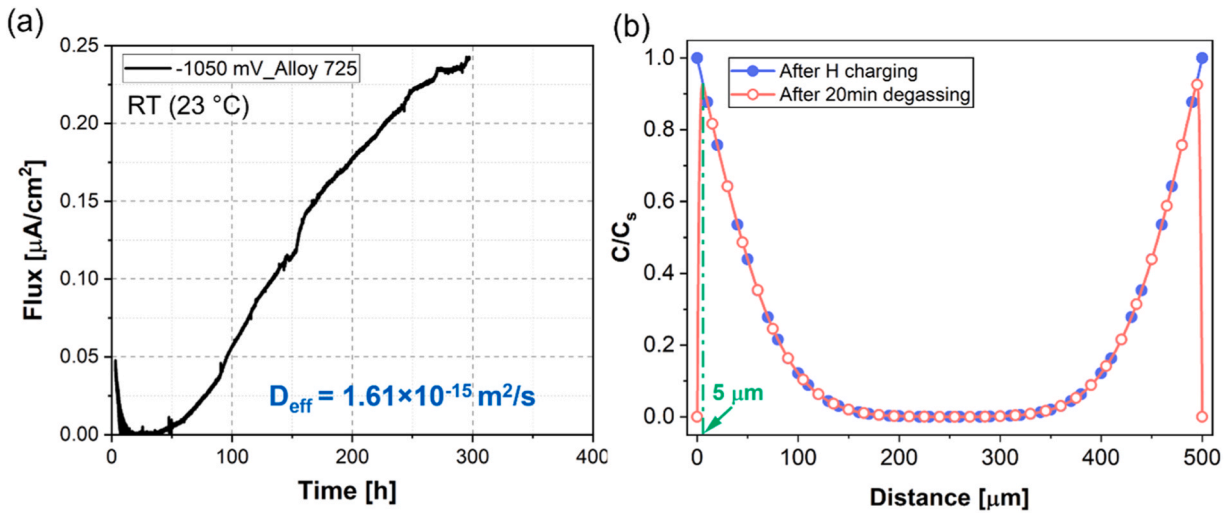

Fig. 1. (a) Electrochemical permeation test on a commercial Alloy 725 at room temperature (23 °C), (b) Hydrogen concentration profiles after hydrogen charging at 75 °C and before tensile testing at room temperature (23 °C, after 20 min of degassing).

With the boundary conditions:

$$C = C_1, x = 0, t \geq 0 \tag{2}$$

$$C = C_2, x = l, t \geq 0 \tag{3}$$

$$C = f(x), 0 < x < l, t = 0 \tag{4}$$

Where C_1 and C_2 refer to the boundary hydrogen concentration on each side, l is the membrane thickness, $f(x)$ describes the initial hydrogen distribution equals to 0, D is the effective diffusion coefficient of hydrogen in the sample. For simplicity, we assume the surface hydrogen concentration to be a constant value C_s. The results are presented by the ratio of $C(x,t)$ to C_s. Therefore, the hydrogen profile after electrochemical charging is shown in Fig. 1(b) (blue curve), where the penetration depth of hydrogen is about 150 μm. In the case of hydrogen desorption before tensile testing, Eq. (1) was used with a constant surface concentration and initial distribution $f(x)$ where $C = \frac{C(x,64800s)}{C_s}$. Hydrogen profile after 20 min of degassing before mechanical testing was added to the charging profile in Fig. 1(b) (red curve), where a drop of hydrogen concentration was observed from the sample surface to 5 μm inward. A comparison of the areas below each concentration profiles shows a reduction of 3.12% in total hydrogen concentration during degassing, which indicates that the majority of hydrogen atoms still remain in the sample. Thus, hydrogen degassing before tensile testing can be neglected.

Tensile tests were performed with an initial strain rate of 2×10^{-5} s^{-1} on a Kammrath & Weiss tensile/compression module installed in a high vacuum chamber (4.7E-3 Pa) inside a high-resolution Quanta FEG 650 scanning electron microscope (SEM, Thermo Fisher Scientific Inc., USA). Both the hydrogen-free and hydrogen-charged samples were deformed until fracture. In addition, to elucidate the role of F phase in fracture process, a sample after 18 h of hydrogen charging was strained before fracture and followed by microstructure characterization.

A post-mortem microstructural analysis of the fractography and surface cracks was conducted using SEM. Electron backscatter diffraction (EBSD) was employed to characterize the cracking behavior at an accelerating voltage of 20 kV with a step size of 0.8 μm. To quantify the hydrogen content in the sample after hydrogen charging, hot extraction tests (G4 Phoenix DH, Bruker Co.) were performed from 50° to 750°C and the data were precisely recorded by mass spectrometry.

2.2. DFT calculation theory

Even though the crystallographic data of F phase was known, obtaining an accurate atomic occupation in F phase crystals, particularly at interface, is still challenging by experimental methods. Therefore, DFT calculations were employed to clarify the atomic structures of both the F phase and interface between the F phase and Ni substrate. Meanwhile, relatively accurate crystallographic sites for hydrogen dissolution were obtained. All DFT [34] calculations were carried out using the Vienna ab initio Simulation Package (VASP) [35]. The exchange-correlation energy functional of the generalized gradient approximation with the Perdew–Burke–Ernzerhof form [36] was adopted in this study. The interaction potential of the core electrons was described using the projector-augmented wave method [37]. The cut-off energy for the plane-wave basis was set to 400 eV. The energy converged to 10^{-6} eV for the self-consistent field calculation. All atoms were allowed to fully relax until the forces on them were less than 0.02 eV/Å. All calculations were performed under spin-polarized conditions.

The crystal structures of the F phase were constructed according to a previous study by Lin and Steeds [27]. The model of the F phase is P6/mmm (with latticed parameters obtained from TEM analysis a = 12.7 Å and c = 4.6 Å, see Section 3.1) and contains nine symmetry-inequivalent positions. According to the chemical composition observed in the experiment (Section 3.1), more than a dozen atomic structures of the F phase were considered with stoichiometric $Fe_4Cr_{24}Mo_{12}Ni_{12}$ when each type of symmetry-inequivalent position was fully occupied by only one type of atom. According to our calculations, the atomic occupancies of the lowest-energy structures are listed in Table 1.

The interface structures between the F phase and Ni substrate were constructed as 1 × 1 F phase unit cells sitting on 5 × 5 unit cells of Ni (1

Table 1
Crystallographic data for the density functional theory (DFT)-calculated F phase.

Wyckoff position	Number	Occupation
c	2	Fe
e	2	Fe
j	6	Ni
k_1	6	Mo
k_2	6	Mo
l_1	6	Cr
l_2	6	Cr
m	6	Ni
o	12	Cr

1 1) (12.57 Å × 12.57 Å × 25 Å) with the strain imposed on the F phase. During geometrical optimization, most of the atoms were allowed to fully relax, while the atoms of the top three layers and the bottom two layers were fixed. The solution energy of a hydrogen atom in an interstitial site was calculated using the following equation:

$$E_{Hsol} = E_{int+H} - E_{int} - 1/2E_{H_2} \quad (5)$$

in which E_{int+H} and E_{int} are the energies after and before the dissolution of the hydrogen atoms, respectively, and E_{H_2} is the energy of a hydrogen molecule.

To determine the interaction characteristics between hydrogen and the interface, $E_{interface}$, the interfacial interaction energies before and after the dissolution of hydrogen atoms, were calculated using the following equation:

$$E_{interface} = (E_{total} - E_{upper} - E_{lower})/S \quad (6)$$

in which E_{total} is the total energy of the interface, E_{upper} and E_{lower} are the energies of the upper and lower parts of the interface, respectively, and S is the area of the interface.

3. Results

3.1. Microstructural analysis of Alloy 725 and identification of F phase

Microstructural characterization of the M1 sample using SEM and EBSD showed a typical polycrystalline face-centered cubic structure with an average grain size of 143.7 μm (Fig. 1(a), excluding twin boundaries). Secondary phases, such as carbonitrides ((Nb, Ti)(C, N)) and aluminum oxide (Al_2O_3) precipitates, can be observed in the matrix. Note that carbonitrides and Al_2O_3 are not anticipated phases during heat treatments based on the time-temperature-transformation diagram of Alloy 725 [38]. In addition, a large fraction of the GBs in Alloy 725 exhibited curved morphologies (yellow lines and arrows in Fig. 2(a)–(b)). A magnified image of the GBs shows heavy decoration of the secondary phases (yellow arrows in Fig. 2(c)), which will be determined as the F phase using TEM and APT approaches in the following sections.

Thorough characterization of the F phase was carried out using TEM and APT. A bright-field image of the F phase at the GB is shown in Fig. 3 (a). This phase is plate-like, with a thickness of approximately 50 nm and a length of ~200 nm. The inverse fast Fourier transform (IFFT) image of the STEM-HAADF image clearly demonstrates that the F phase has a coherent interface with the γ matrix, exhibiting continuous lattices across the phase boundary (Fig. 3(b) and (c)). However, an incoherent interface with the matrix on the other side is anticipated and has been reported in Ref. [28] to accommodate the crystallographic misorientation in the adjacent grains. Similar to the σ phase, the F phase was found to be highly faulted. The TEM sample was tilted to reach two zone axes, $[011]_\gamma$ and $[\bar{1}12]_\gamma$, in the left grain of the γ matrix (Fig. 3(a)). The recorded SAD patterns in Fig. 2(d) and (f) show the typical diffraction patterns of the face-centered cubic structure along the $[011]_\gamma$ and $[\bar{1}12]_\gamma$ zone axes. Reflections from the superlattice structures were identified as the γ'' phase. Correspondingly, NBD patterns were recorded in the F phase at the zone axes of $[2\bar{1}\bar{1}0]_F$ and $[1\bar{1}00]_F$ (Fig. 3(e) and (g)), following the tilting conditions of the γ matrix. The diffraction indexation was compared with the simulated kinematic electron diffraction patterns for possible precipitate candidates reported in the literature. This result was consistent with that of the F phase (hexagonal, D^1_{6h}, *P6/mmm*) with measured lattice parameters of a = 12.7 Å and c = 4.6 Å. The defined F phase/γ matrix orientation relationship is in good agreement with that of a recent study [28]:

$$(0001)_F // (1\bar{1}1)_\gamma$$

$$[2\bar{1}\bar{1}0]_F // [011]_\gamma$$

The three-dimensional (3D) atom map of the γ matrix splitting by a GB was obtained from ATP analysis, as shown in Fig. 4(a). The F phase on the top part of the APT tip shows a plate-lie morphology that deflects the GB path (Fig. 4(a)), which agrees well with the SEM micrograph in Fig. 2(c). Further, the F phase was attached to some γ'' phases. The compositional profile along the interface between the γ'' and F phase (Fig. 4(c)) manifests an enrichment of Cr, Mo, and Fe in the F phase. Likewise, another compositional profile along the F phase/matrix interface shows surplus Cr and Mo and the depletion of Ni, Nb, Al, Si, and Ti in the F phase compared with the matrix (Fig. 4(d)–(e)). The average values of the primary chemical compositions in the F phase obtained from the APT reconstruction are listed in Table 2.

In contrast, the micrograph of the M2 sample shows clean GBs free of the F phase (Fig. 5(a)) with an average grain size of 150.1 μm. The STEM-EDS mapping on an arbitrary GB demonstrates the segregation of B and Mo and depletion of Ni along the GB, as indicated by the yellow arrows in Fig. 5(b)–(f). In addition, EDS line scanning perpendicular to the GB shows results parallel to the mapping (Fig. 5(g)). The magnified image in the inset clearly reveals B and Mo enrichment as well as Ni depletion. There is no clear evidence of Cu inhomogeneity.

3.2. Hydrogen impact on two modified alloys

Fig. 6 shows the stress-strain curves obtained under both hydrogen-free and hydrogen-charged conditions for the two modified samples. Hydrogen induced a reduction in the yield stresses of approximately 2.8% and 3.8% in the M1 and M2 samples, respectively. However, the elongation reduction decreased significantly from 91.8% to 75.7%, indicating a higher resistance to hydrogen-assisted degradation in the M2 sample. Worthy of note, hydrogen degassing before tensile testing only accounts for 3.12% of the total hydrogen concentration. In addition, hydrogen concentration of M1 sample was 23.28 wppm (1415.89

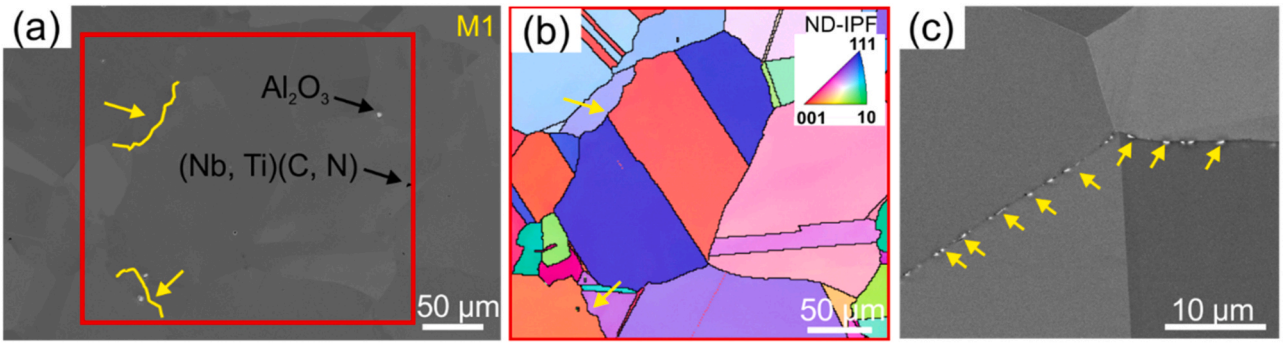

Fig. 2. (a) Microstructure of M1 sample and (b) corresponding inverse pole figure map of area marked by red box in (a), (c) backscattered electron (BSE) image showing precipitate-decorated GB.

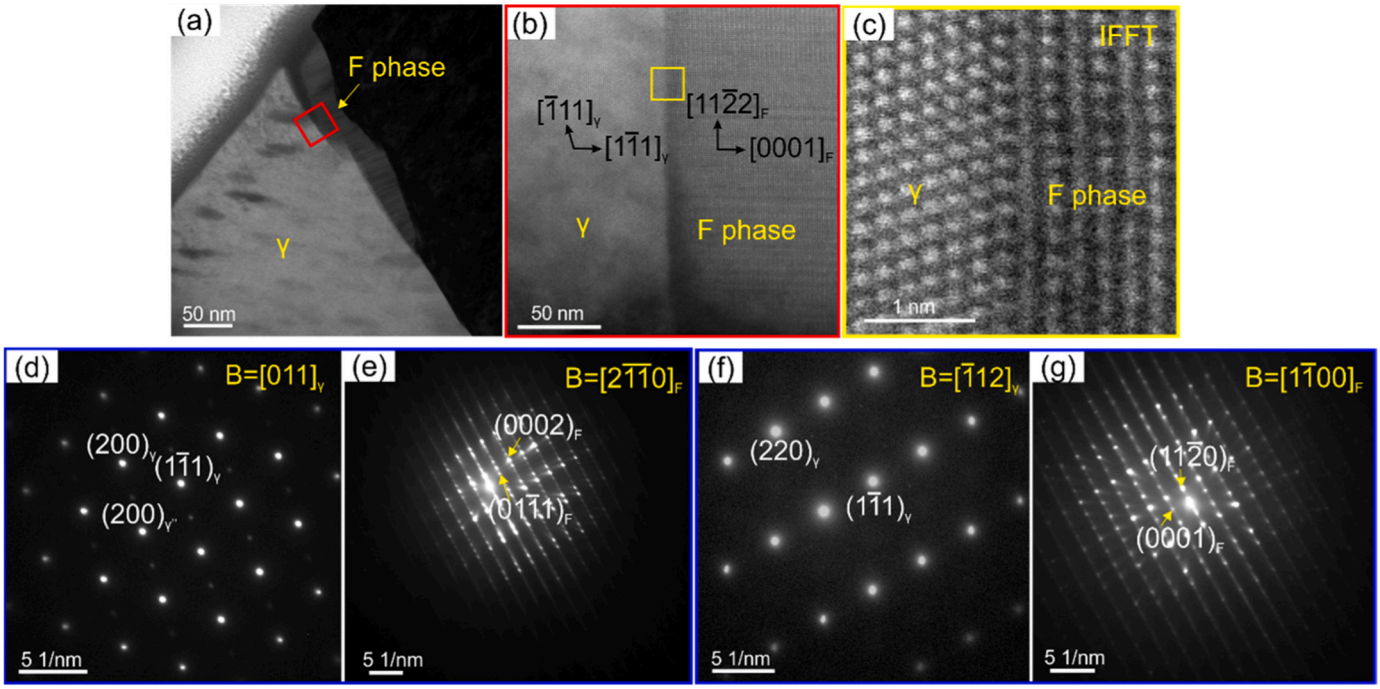

Fig. 3. (a) Bright-field TEM micrograph of GB F phase, (b) STEM-HAADF imaging of coherent F/ γ phase boundary, (c) IFFT image of HAADF enclosed by yellow box in (b), (d) and (f) SAD patterns of left γ grain tilted at zone axes$[011]_\gamma$ and $[\bar{1}12]_\gamma$, respectively, and (e) and (g) NBD patterns of F phase at zone axes of $[2\bar{1}\bar{1}0]_F$ and $[1\bar{1}00]_F$ following tilting conditions for γ matrix.

appm) measured by hot extraction test, which indicates the reduction in mechanical properties is induced by hydrogen-assisted premature fracture.

Fig. 7 shows the fractography of the M1 sample. The hydrogen-free condition demonstrated a typical ductile failure mode realized through microvoid coalescence (Fig. 7(a)). A striking feature in Fig. 7(a) is the evidence of intergranular fractures reflecting the weakness of the GB (Fig. 7(a1)−(a2)). In the hydrogen-charged condition, intergranular fractures manifested as the prevailing failure mechanism in the outer brittle region (Fig. 7(b)−(b2)), demonstrating the high susceptibility of the GB to cracking with hydrogen occlusion. Interestingly, a magnified cracked GB facet (marked by blue lines) revealed the existence of abundant irregularly shaped microvoids (Fig. 7(c2)). One can easily distinguish that these voids are unlike the triangular ones, which originate from the intersections of dislocation slip bands during plastic deformation (black box in Fig. 7(c)). The measured average size of the microvoids on the fractography was approximately 250 nm, which coincides with the size of the F phase probed by APT and TEM, indicating that these voids are the result of the cracking of the F phase interfaces. In addition, to demonstrate the deleterious effect of the F phase, the surface primary cracks and secondary cracks after loading to fracture in the hydrogenated M1 sample were characterized by EBSD. In Fig. 8, the SEM and inverse pole figure maps clearly reveal the intergranular-dominant cracking behavior marked by arrows in Fig. 8(b)−(c). Cracking at the F phase interface can be observed in the inset (yellow arrows in Fig. 8(d)). The crack propagates and stops at the twin boundary, where a deficiency in the F phase is observed. Direct evidence of the role of F phase in hydrogen-interplayed fracture behavior is shown in Fig. 9, where the sample was strained to approximately 2% (Fig. 9(a1)). Backscattered electron (BSE) image shows a complete intergranular cracking of the strained sample. High resolution secondary electron (SE) and BSE images of grain boundaries clearly demonstrate microvoids nucleation at F phase interfaces (Fig. 9(b)−(g)). The coalescence of these microvoids leads to the decohesion of grain boundaries, as shown in Fig. 8(d). As F phase heavily precipitates along the grain boundary, the cracking of these grain boundaries coalescences and the crack propagates intergranularly (Fig. 9(a)).

In comparison, the fractography of the M2 sample in Fig. 10 shows typical ductile dimples covering the entire fracture surface with no evident intergranular cracking under hydrogen-free conditions (Fig. 10 (a)). Under the hydrogen-charged condition, a mixture of intergranular and transgranular cracking was detected in the brittle region, the majority of which exhibited transgranular features (Fig. 10(b)). Moreover, the majority of surface secondary cracks shows transgranular fracture at dislocation slip band intersection, which is a typical failure mode in nickel alloys (Fig. 10(c)−(d)).

3.3. DFT results

During hydrogen charging and tensile testing, hydrogen atoms can be trapped or moved toward the F phase/matrix interfaces. The hydrogen solution energies at different interstitial sites at the interface between the F phase and Ni substrate were determined by DFT calculations. Fig. 11(a) shows the atomic structures of hydrogen atoms at different interstitial sites. Specifically, S1−S5 illustrate the hydrogen atoms dissolved in the interstitial sites at the F phase/Ni matrix interfaces. S6 and S7 show hydrogen trapped at tetrahedral sites, whereas S8 and S9 are trapped at octahedral sites. According to the calculations, six types of interstitial sites at the interface are stable hydrogen traps with negative solution energies (S1, S2, S3, S4, S5, and S8 in Fig. 11(b)).

These stable states were used for further $E_{interface}$ calculations. It was demonstrated that the initial $E_{interface}$ in the hydrogen-free structure is − 250.1 meV/Å^2, which is stronger than those of the interfaces with hydrogen dissolution, as shown in Fig. 11(c). Furthermore, the interfacial interaction characteristics can be inflected by the hydrogen atoms. It needs to mention that the interfacial interaction energy can be both positive and negative values, based on the formulation of Eq. (6) [39–42]. Typically, the absolute value of interface energies that were used to measure the stability of the interface structure and thus the bonding strength. These results successfully corroborate the experimental observations by indicating that the dissolution of hydrogen atoms weakens the binding strength of the interfaces between the F

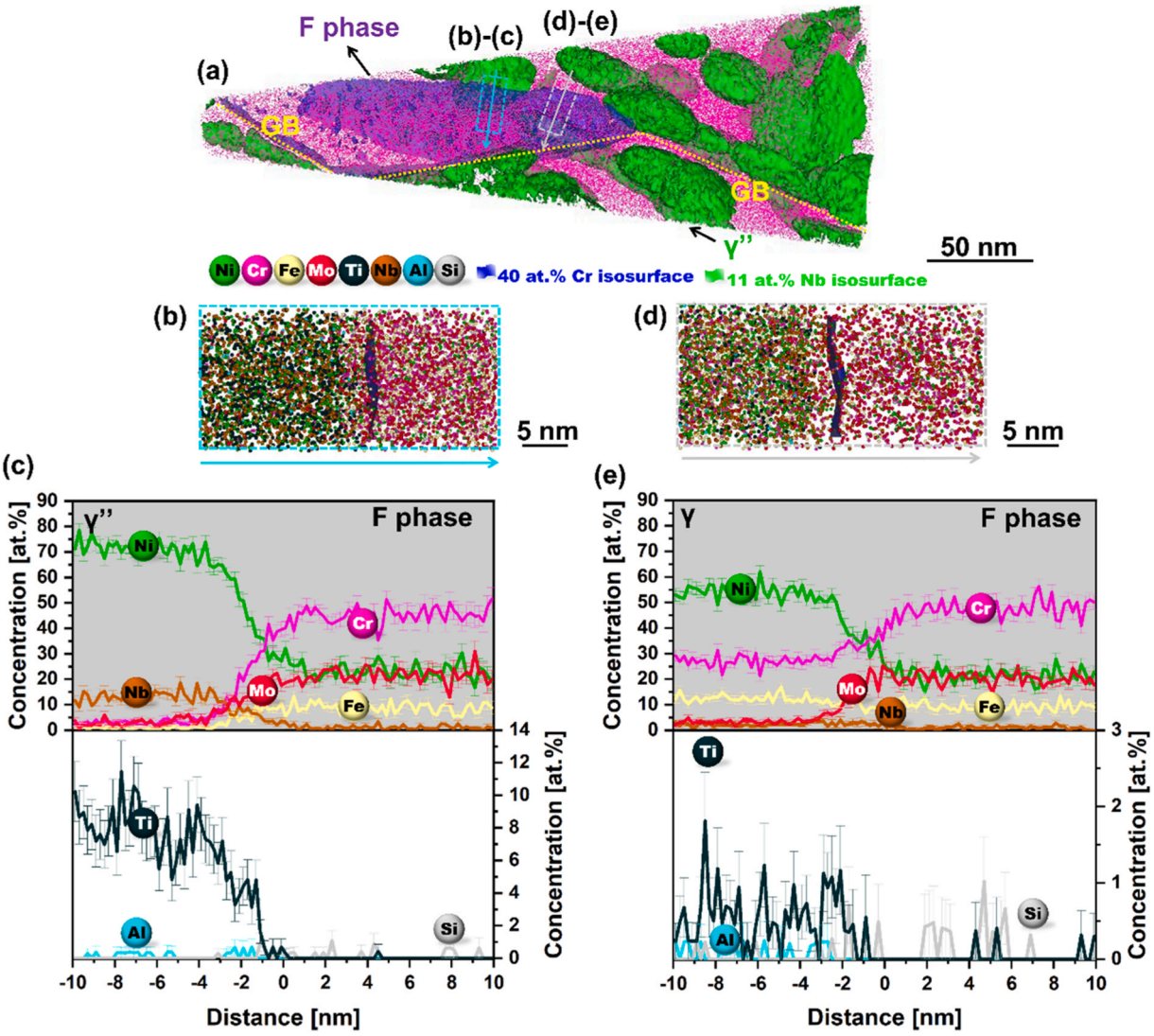

Fig. 4. Atom probe tomography analysis: (a) 3D atom map of M1 sample matrix containing GB, (b) enlarged atom map and (c) corresponding 1D concentration profile along the selected region of interest (ROI) marked in light blue, (d) enlarged atom map and (e) 1D concentration profile along the selected ROI marked in gray. (For interpretation of the references to color in this figure legend, the reader is referred to the web version of this article.).

Table 2
Average chemical composition of primary elements in F phase obtained from APT analysis.

F phase	Chemical composition (at%)			
	Ni	Cr	Mo	Fe
APT	21.61 ± 2.41	47.78 ± 2.93	20.44 ± 2.35	9.09 ± 1.68

phase and Ni matrix. It needs to mention here that only the coherent interface was accounted for DFT calculations. However, it still provides valuable information for interpreting the decohesion behavior by hydrogen dissolution into the F phase/Ni matrix interface.

In addition, the hydrogen solution energies in the F phase (21 tetrahedral sites) and Ni matrix (both octahedral and tetrahedral sites) were calculated and listed in Table 3. From Table 3, the lowest solution energy for hydrogen atom in the F phase is tetrahedral site nr.3, with a corresponding value of 0.22 eV. The solution energies for hydrogen in the Ni matrix are 0.08 eV and 0.35 eV for the octahedral and tetrahedral sites, respectively. A schematic showing hydrogen atom dissolved in nr.3 tetrahedral site in the F phase is demonstrated in Fig. 12 (a). Compared to the solutions energies of hydrogen at the F phase/Ni matrix interface (Fig. 11(b)), the interstitial sites at both the F phase and Ni matrix are not stable hydrogen trapping sites, and the interfaces are the most stable trapping sites for hydrogen atoms. Furthermore, using the solution energy of hydrogen atom at interfacial interstitial site S3 (−0.12 eV, Fig. 11(b)), the system energy change when hydrogen diffuses through the path: octahedral site in the Ni matrix → interface → tetrahedral site in the F phase was calculated and shown in Fig. 12(b) and (c). Taking the system energy of hydrogen dissolved in the Ni matrix as zero, two energy barriers can be identified (0.36 eV and 0.2 eV). It demonstrates that hydrogen atom trapped at the F phase/Ni matrix interface (S3 site) needs to overcome energy barriers of 0.52 eV and 0.36 eV to diffuse towards the Ni matrix and F phase, respectively. Therefore, in both thermodynamic and kinetic perspectives, the calculations indicate that hydrogen tends to stably dissolve (be trapped) at the interface.

4. Discussion

4.1. Deleterious effect of F phase in hydrogen-free samples

The most prevalent phases in nickel-based alloys are the matrix gamma phase (γ) and the strengthening phases γ' and γ''. However,

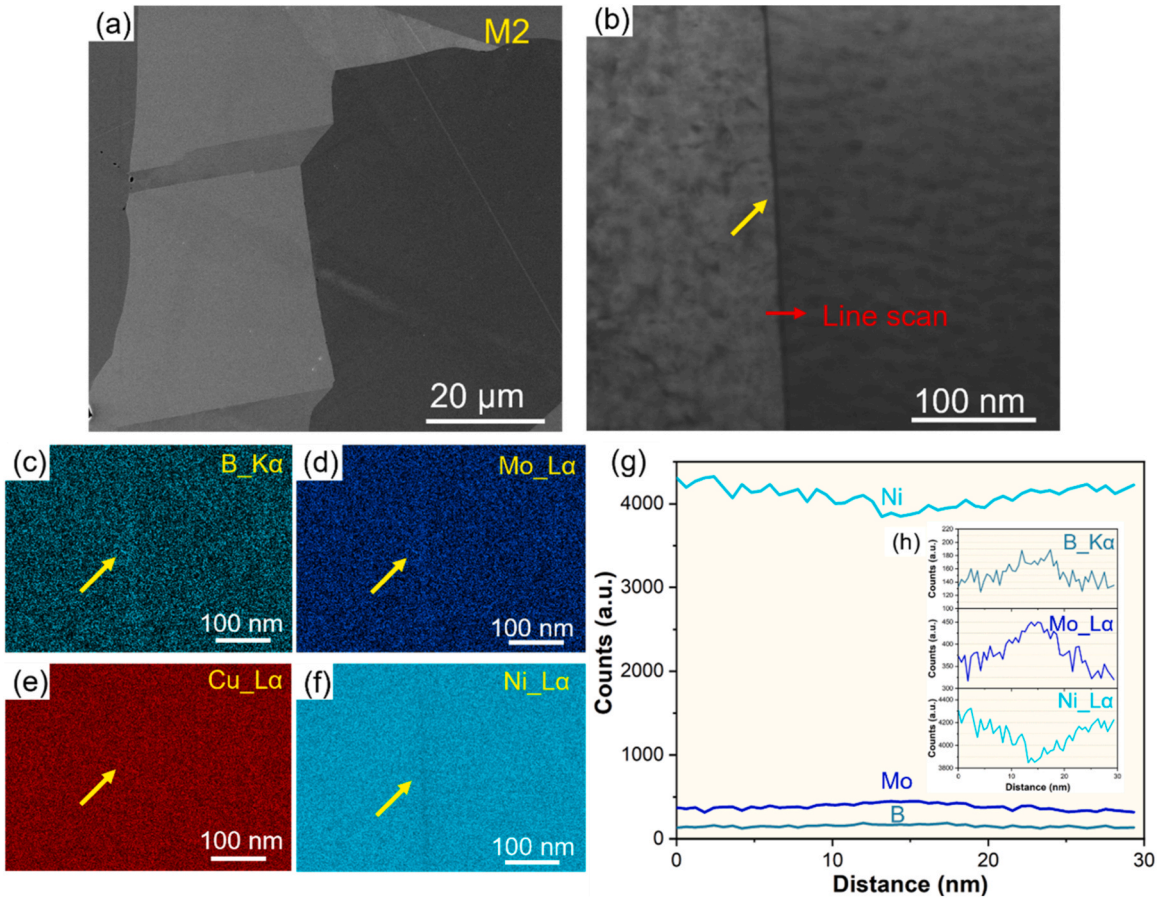

Fig. 5. (a) Microstructure of M2 sample, (b) STEM image of selected GB for EDS scan, (c)−(f) EDS mappings show segregation of B_Kα, Mo_Lα and depletion of Ni_Lα along GB, and (g) EDS line scan perpendicular to GB and magnified results in insets.

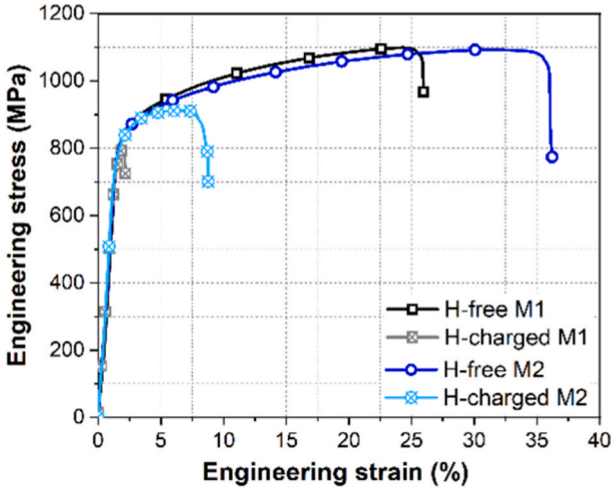

Fig. 6. Hydrogen effect on engineering stress-strain curves of two modification Alloy 725 samples.

excessive concentration of refractory elements promotes the formation of TCP phases, for example, the σ, μ, and Laves phases, which are hard and brittle and typically precipitate during prolonged exposure at elevated temperatures [43,44]. Their formation results in the depletion of refractory elements from the γ matrix, thereby reducing its strength. The large mechanical contrast between γ matrix and TCP phases, e.g., a 7 GPa difference in nanohardness [45], leads to a high potency toward initiating cracking. Thus, the TCP phases are detrimental to the mechanical properties.

Nonetheless, the TCP-related intermetallic F phase remains unelucidated. Hazarabedian *et. al.* [28] reported that the F phase exhibits a semi-coherent or incoherent interface with the γ matrix and grows parallel to the $(111)_\gamma$ plane by forming either continuous or discontinuous sheets based on the crystallographic orientation between the $(111)_\gamma$ plane and GB. In this study, the F phase and γ matrix share the orientation relationship of $(0001)_F//(1\bar{1}1)_\gamma$, and cohabit on a coherent interface exhibiting a straight morphology with the matrix on one side of the grain. However, an incoherent interface with the matrix on the other side is anticipated to accommodate the crystallographic misorientation in the adjacent grains. This observation again indicates that the F phase nucleates preferably, where the $(111)_\gamma$ plane is parallel to the GB. Analogous to the σ phase, the segregation of Cr and Mo in the F phase causes local enrichment of Nb in the exterior zone, where the nucleation of γ'' attached to the F phase is promoted (Fig. 3(a)).

Similar to the other frequently observed TCP phases and carbides at GBs [43,46,47], the plate-like F phase exhibits an embrittlement effect and causes intergranular cracking in nickel-based alloys even under hydrogen-free conditions. Recent molecular dynamics simulations on Σ11 GB in a Ni-Al alloy have shown that a certain amount of coherent γ' could alter the GB shear mechanism from local atomic shuffling to dislocation emission [48], meanwhile increasing the residual strain induced by the phase misfit. Typically, the binding strength between the precipitate and matrix is directly related to the coherency level of the interface, where a higher coherency indicates a higher interfacial strength. It has been demonstrated that the F phase and γ matrix share a coherent interface with one grain and an incoherent interface with the adjacent grain, a higher potency of vacancy formation and more

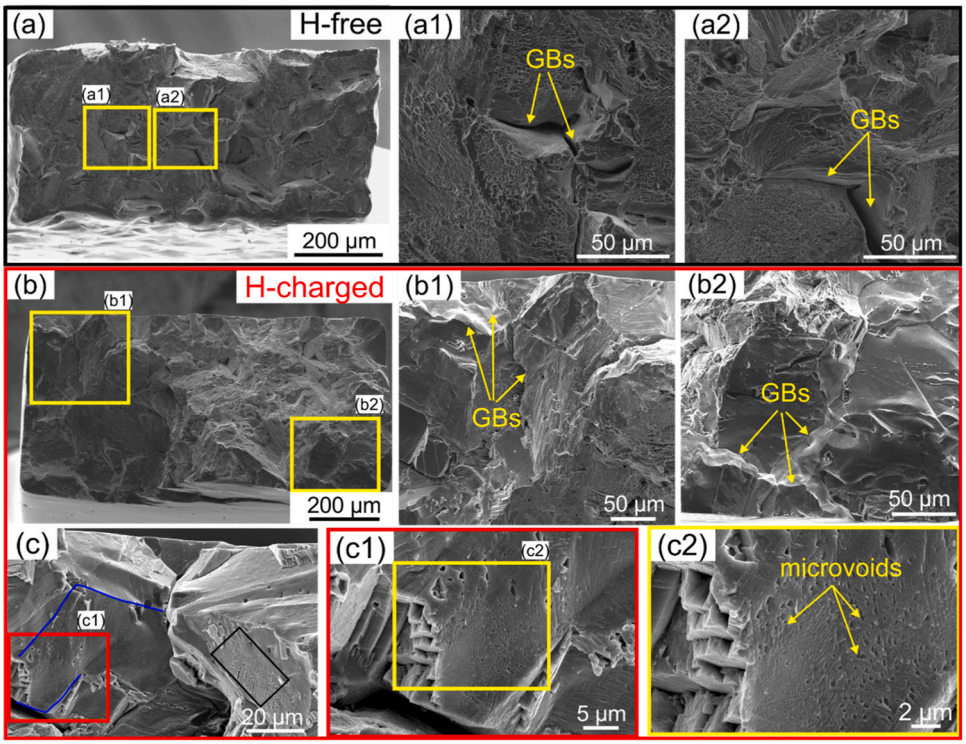

Fig. 7. Fracture surface of M1 sample tested in (a) hydrogen-free (H-free) condition, showing (a1)–(a2) GB cracks, (b) hydrogen-charged (H-charged) condition with (b1)–(b2) intergranular cracks, and (c)–(c1) details of intergranular cracking in M1 sample with a magnified area enclosed in (c2) exhibiting irregularly shaped microvoids.

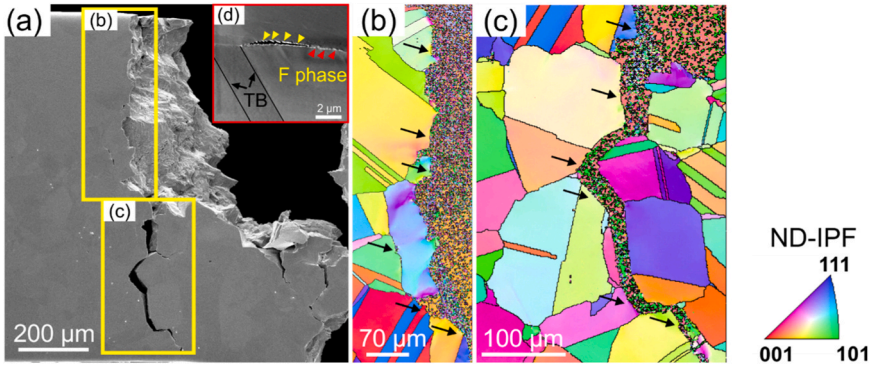

Fig. 8. (a) SEM micrograph of M1 sample surface cracks in hydrogen-charged sample after fracture, and corresponding (b)–(c) inverse pole figure maps of highlighted areas in (a), and (d) cracking along the F phase-decorated GB. TB represents twin boundary.

dislocation nucleation could be foreseen, considering the apparent difference in lattice constants and, possible substantial discrepancy in their strength, and the disordered structures at the interfaces. Therefore, a higher strain level at the F phase/Ni matrix interfaces compared with that of the normal GBs upon straining is anticipated. In addition, the precipitation of the F phase increased the tortuosity of the GB and led to more stress concentrators during plastic deformation. All of these factors render the F-phase-decorated GBs favorable sites for crack initiation and propagation (Fig. 9).

4.2. Synergistic effect of hydrogen and F phase

The section above demonstrates that the F phase alone can be a source of cracking, acting as a potential threat to the application of Alloy 725. When hydrogen, an embrittling element, was introduced into the system, a drastic degradation in the mechanical properties was observed (Fig. 6).

During electrochemical hydrogen charging, in addition to the lattice sites, crystallographic defects such as dislocations, GBs, precipitates, and vacancies trap hydrogen. The trap occupancy fraction was primarily controlled by the trapping energy of the different traps and the applied temperature. Table 4 summarizes F phase and the commonly investigated defects in Ni alloys and their corresponding binding energies based on both experimental and simulation investigations. Note that the precipitates in Table 4 refer only to the reversible traps γ', γ'', δ, and $M_{23}C_6$.

In addition, The F phase and Ni matrix exhibit a coherent interface with one grain and an incoherent interface with the adjacent grain [28]. DFT calculations show that the detrapping energy (trap activation energy) of hydrogen atoms from the interface toward Ni matrix refers to the energy required to overcome the energy barrier shown in Fig. 12 (c), which is 0.52 eV. Based on the solution energy of hydrogen atom in the Ni matrix (0.08 eV) and taking the S3 interstitial site as the most stable trapping site (−0.12 eV), the binding energy between the coherent F

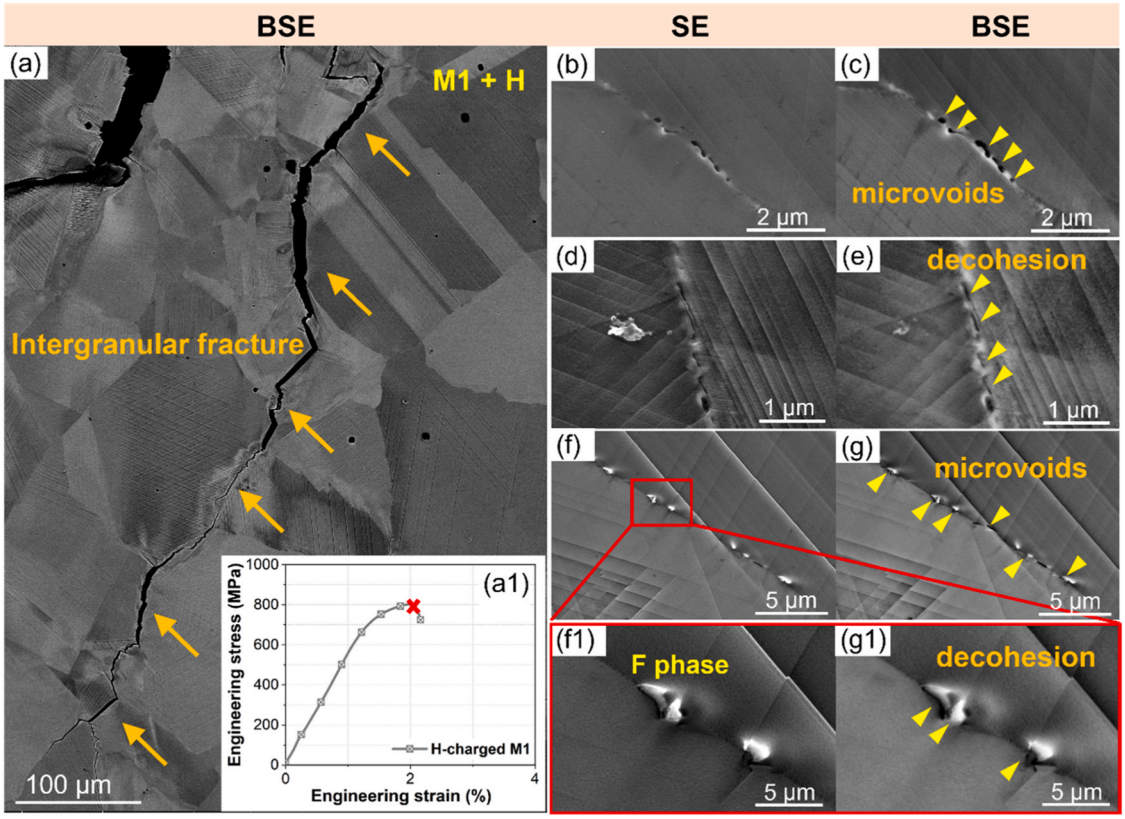

Fig. 9. (a) BSE image of surface secondary cracks of M1 alloy that was strained before fracture after hydrogen charging for 18 h (as illustrated in (a1)) demonstrating a complete intergranular fracture feature, (b)-(g) secondary electron images and corresponding BSE images of F phase-decorated grain boundaries showing both microvoids nucleation and decohesion at F phase interfaces, (f1) and (g1) are magnified images of (f) and (g).

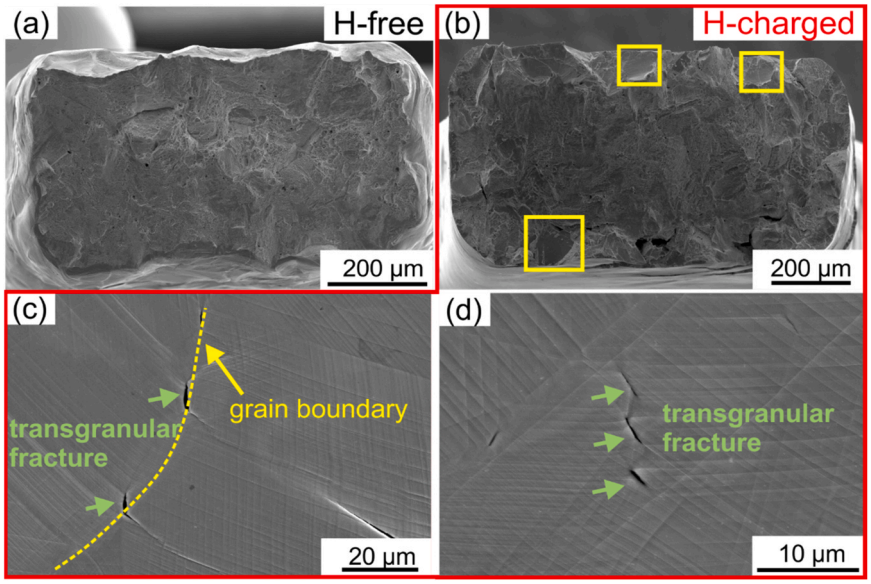

Fig. 10. Fracture surface of M2 sample tested in (a) hydrogen-free (H-free) condition and (b) hydrogen-charged (H-charged) condition, where intergranular cracks are enclosed in yellow boxes, (c)-(d) Surface secondary cracks in hydrogen-charged sample showing a transgranular fracture dominant feature.

phase interface and hydrogen is − 0.2 eV. Therefore, F phase/Ni matrix interface is served as reversible trapping site for hydrogen atoms. Consistent with the literature, a coherent interface has been reported as a reversible trap for hydrogen [49,50], and a diminution in coherency effectively increases the trap binding energy. Considering that an equilibrium state is reached between the trapped and lattice hydrogen atoms, where hydrogen hops between different trap sites are neglected, the occupancy fraction of traps can be derived from the McLean segregation isotherm [51,52]:

$$\frac{\theta_T}{1-\theta_T} = \theta_L \exp\left(\frac{-E_b}{RT}\right) \tag{7}$$

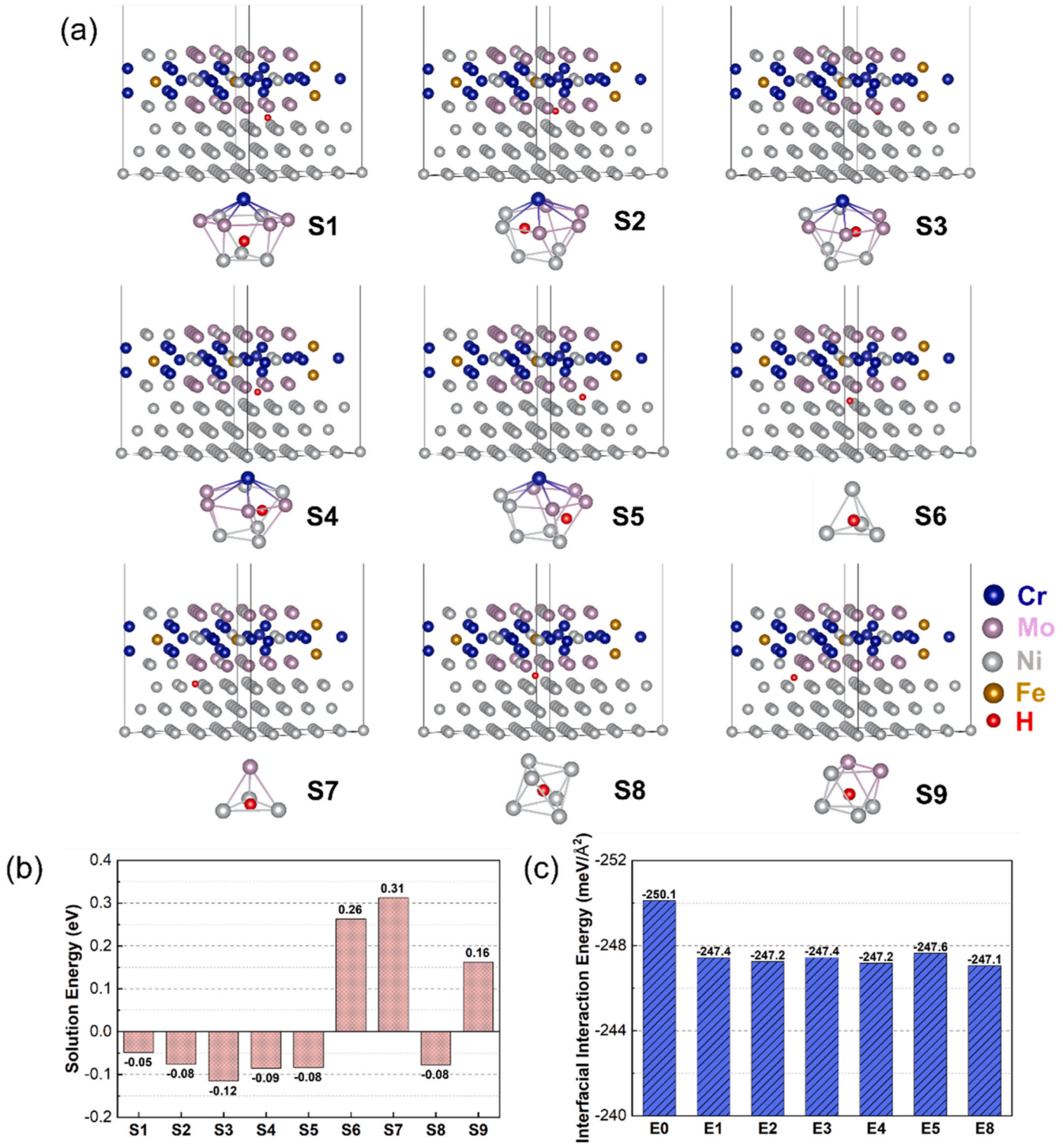

Fig. 11. Hydrogen solution behaviors at interstitial sites of interface between F phase and Ni: (a) atomic structures of hydrogen atoms in different interstitial sites; S1−S5 illustrate hydrogen atoms trapped at the interfaces between F phase and the matrix and S6−S7 illustrate hydrogen atom at tetrahedral sites, and S8−S9 at octahedral sites, (b) solution energies of H atom in different interstitial sites, and corresponding (c) interfacial interaction energies. E0 is interfacial interaction energy of interface without dissolution of hydrogen atom.

Here, θ_T is the trap site occupancy and θ_L is the lattice site occupancy, and is equivalent to the total lattice hydrogen concentration in appm ($\theta_L \ll 1$) with some simple assumptions: one hydrogen atom in an one-trap site and an O-site is occupied [53], E_b is the binding energy (eV) of the corresponding traps, R is the Boltzmann constant, and T is the hydrogen charging temperature (K). In this study, θ_L was measured from hot extraction test to be 23.28 wppm (1415.89 appm). Accordingly, the evolution of the hydrogen occupation fraction at different traps is depicted in Fig. 13, where the gray arrow refers to an increase in the binding energy. Based on the SEM and TEM observations, there is no clear evidence for the noticeable amounts of microvoids, dislocations, and vacancies. Although the F phase is in a faulted state, the fraction of

Table 3
Solution energies of hydrogen atom in 21 types of tetrahedral sites (T-site) in the F phase, and in both the octahedral site (O-site) and tetrahedral site (T-site) in the Ni matrix.

F phase				Ni (γ) matrix	
Site (T-site)	E_{Hsol} (eV)	Site (T-site)	E_{Hsol} (eV)	Site	E_{Hsol} (eV)
1	1.02	12	1.12	O-site	0.08
2	0.29	13	0.75	T-site	0.35
3	0.22	14	0.97		
4	0.92	15	1.22		
5	0.98	16	0.78		
6	0.92	17	1.00		
7	0.92	18	1.35		
8	1.22	19	1.05		
9	0.76	20	1.16		
10	0.79	21	1.07		
11	0.97				

stacking faults is negligible compared to the bulk microstructure. Based on the binding energy of hydrogen at the F phase/Ni interface shown in Table 4 (−0.2 eV), the critical value of hydrogen occupancy fraction at interface is 0.53 in an equilibrium state, indicating a relatively high hydrogen occupancy at octahedral trapping sites after hydrogen charging.

During electrochemical hydrogen charging, hydrogen atoms are absorbed into the sample, and some are trapped at the F phase/Ni matrix interfaces [63]. The diffusible hydrogen was claimed as the reason for the embrittlement of a metal. However, the reversibly trapped hydrogen is important as well because hydrogen atoms can hop between the lattice and trap sites when the sample is under deformation, where the atom exchange between lattice and the reversible trap sites can be thermodynamically promoted. During plastic deformation at a relatively slow strain rate, diffusible hydrogen can migrate with geometrically necessary dislocations toward the GB and form pileups. Hydrogen atoms moving to the F phase can be trapped at the interfacial interstitial sites because of the low solution energy and in the tensile strain fields in the nearby matrix [64]. Compared to the previously trapped hydrogen at the interface, hydrogen thermal fluctuations at locations with high dislocation densities, such as dislocations piling up at interfaces and GBs, cause hydrogen concentration high enough to initiate cracks, which can be a critical reason for the intergranular fracture [65]. Additionally, dynamic hydrogen-dislocation interactions at the interface elevate local stress and facilitate crack initiation. As corroborated by the DFT calculations, hydrogen dissolution at the F phase interface can substantially reduce the interfacial interaction energy in all simulated stable trapping states and promote intergranular cracking. This phenomenon is successfully supported by the hydrogen-enhanced decohesion mechanism [66–68] and "Defactant" theories [20,21,69]. We clearly demonstrated that in the presence of hydrogen, the very first cracks nucleated at the F phase/Ni matrix interfaces but rather at clean grain boundaries. The F phase/Ni matrix interfaces are thus more susceptible to hydrogen-assisted cracking than precipitation-free grain boundaries. In addition, during plastic deformation, the local mechanical contrast between the F phase and abutting matrix caused stress elevation at the interface and attracted more hydrogen atoms. A much higher stress was reached at the interface during dislocation multiplication and interactions. The formation of strain-induced vacancies could also be promoted at interfaces [70]. The synergistic effect of the above factors caused the local stress intensity to quickly reach the critical value needed to initiate microcracks. It needs to be mentioned that the hydrogen solution energy we calculated refers to the coherent F phase/Ni matrix interface. It is known that incoherent interface is more critical in trapping hydrogen and facilitating hydrogen-related intergranular fracture. In the current study, TEM results provide detailed crystallographic data only on coherent interface, but rather incoherent one. Therefore, hydrogen solution energy of only coherent interface is considered in the DFT calculations. It is thus of great importance in future study to carry out detailed experimental analysis and calculations

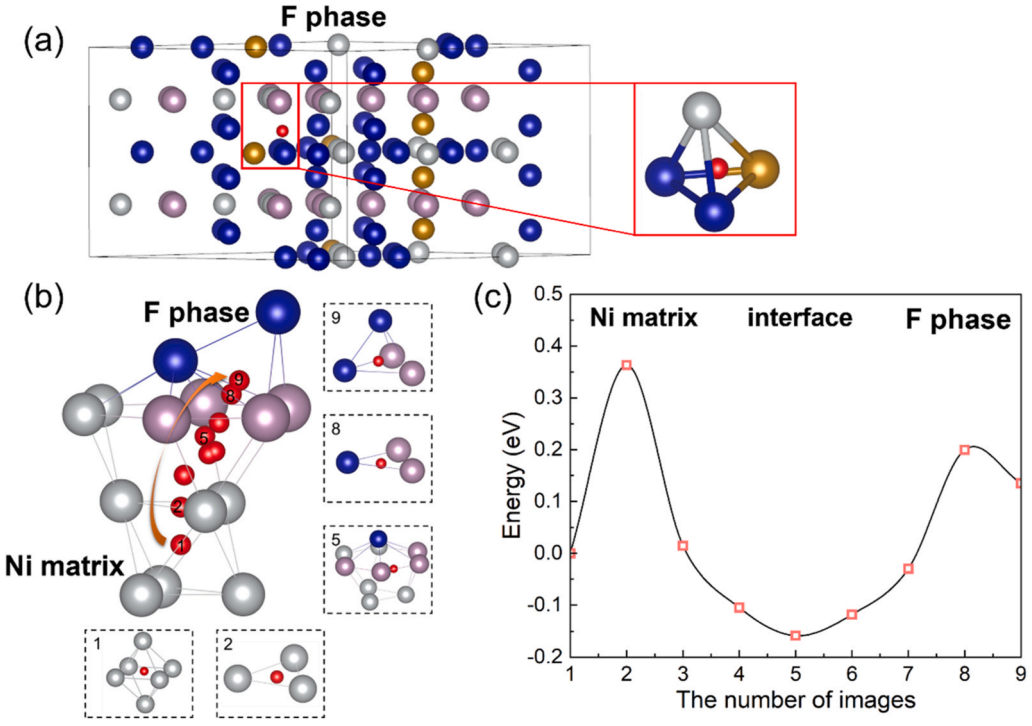

Fig. 12. Schematic showing (a) hydrogen atom occupies tetrahedral site with the lowest solution energy (nr.3 in Table 3) in the F phase, (b) hydrogen diffusion process from octahedral site in the Ni matrix through the interface interstitial site S3 (Fig. 11(b), solution energy − 0.12 eV) and further to the tetrahedral site in the F phase, detailed occupation sites in enlarged images, (c) corresponding energy change in the diffusion process, taking the system energy of hydrogen dissolved in Ni matrix as zero.

Table 4
Literature summary of binding energies between crystallographic features and hydrogen in Ni. Here MD and TDA represent molecular dynamics and thermal desorption analysis, respectively.

Microstructure feature	Binding energy, eV	Method, crystallographic type
Dislocation	-0.10[54]	MD, screw/edge dislocation
Stacking fault	-0.075[54]	MD, < 112 > (111)
Grain boundary	-0.23~− 0.31[18, 55–57]	DFT, Tilt ∑5(012)
	-0.16[58]	DFT, Twist ∑5(001)
	-0.21[53]	TDA, General grain boundary
Vacancy	-0.25[18]	DFT, Mono-vacancy
Precipitate	-0.32~− 0.38[59]	Electrochemical permeation, γ'
	-0.20[60]	Nuclear reaction analysis, γ'
	-0.31[59]	Electrochemical permeation, δ
	-0.24–0.28[59]	Electrochemical permeation, γ''
	-0.20~− 0.29[61]	TDA, $M_{23}C_6$
	-0.72[62]	TDA, σ
F phase/Ni matrix interface (coherent)	-0.2 [this work]	DFT
Microvoid (H at surface)	-0.60[18]	DFT, (012) free surface
	-0.58[58]	DFT, (001) free surface

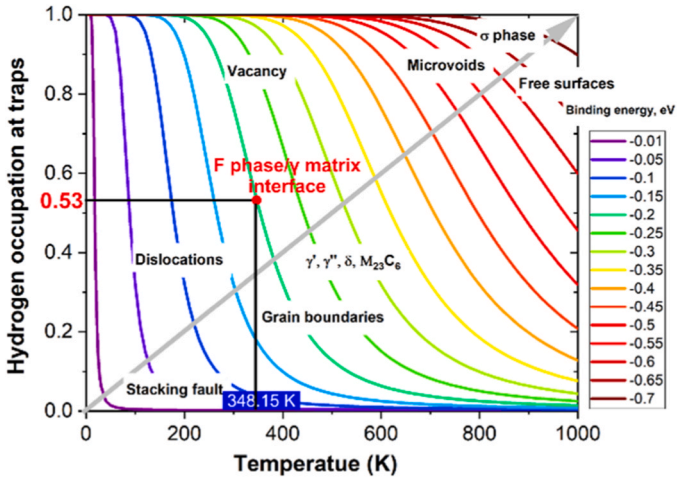

Fig. 13. Calculated hydrogen occupation at traps adopted from McLean segregation isotherm. Gray arrow refers to augment of binding energy. Hydrogen occupation at the F phase/Ni phase interface is 0.53 at 348.15 K.

on incoherent interface to comprehensively reveal the hydrogen-related intergranular cracking. Still, current study provides valuable insights in the hydrogen-induced fracture mechanisms of nickel alloys containing grain boundary precipitates.

Moreover, similar to the sulfur (S) segregation at GBs by forming bipolar interfacial structures and causing embrittlement in nickel [71], the zig-zag morphology of F-phase-decorated GBs (Fig. 4) are favorable sites for cracking under hydrogen occlusion. It needs to mention that even though the intergranular fracture has also been reported to occur at precipitation-free grain boundaries [14], where the correlation between grain boundary character and fracture was thoroughly discussed, the objective of this work is to highlight the role of F phase in its early initiation of intergranular fractures compared with precipitation-free grain boundaries in the presence of hydrogen. All the results show that the existence of F phase is of significant importance and raises the need for the re-evaluation of this alloy for subsea applications, where hydrogen embrittlement remains a critical issue under cathodic protection.

4.3. Overcoming the GB embrittlement thorough alloy design

A possible approach to reducing the formation of the F phase via thermal and thermomechanical treatments has recently been proposed for manufacturing nickel alloys with better properties in a hydrogen environment [72]. However, service conditions can promote additional aging effects and lead to the formation of the F phase during service. Herein, we propose a new alloying approach to eliminating the nucleation of F phase by doping with B. It was demonstrated that only a minor addition of B to the alloy system could effectively suppress the precipitation of the F phase. Instead, B and Mo segregation at the GBs was accompanied by Ni depletion (Fig. 5). The deficiency of the F phase at the GBs enhances the ductility of the alloy by 39.0%, whereas it has little effect on the alloy strength (Fig. 6). More exalting, in the hydrogenation environment, the M2 sample with B doping revealed much higher ductility compared with the M1 sample, with an increase of 16.1% in elongation reduction.

Under hydrogen-free conditions, many studies have investigated the effects of B segregation on GB cohesion in metallic materials, especially for creep and fatigue applications. For instance, the segregation of B on high-angle GBs was found to enhance GB cohesion and improve the mechanical properties of a creep-resistant polycrystalline Ni alloy when used at up to 700 °C [73]. In steel, DFT calculations suggest that the cohesive energy of the Fe Σ3(111) symmetrical tilt GB increases by 1 J/m^2 owing to the segregation of B [74]. Based on the model proposed by Briant and Messmer [75], B is less electronegative with respect to the base metals and cannot draw charge from the neighboring metal atoms but rather shares electrons with them. Instead of weakening the metal−metal bonds, the segregation of B enhances the atomic bonds at the GBs [76]. In addition to the benefits of an elevated GB cohesive strength, other strengthening mechanisms have also been proposed. For instance, B could delay the segregation of the embrittlement element S at GBs, thereby reducing the propensity for intergranular cracking of a nickel-based superalloy [77]. DFT calculations demonstrated the strong segregation of B toward the Ni ∑5(012) GB, which could potentially prevent the segregation of other undesirable solutes and prevent damage initiation [78]. B was also reported to be able to lower both the GB diffusivity and void nucleation rate by filling vacancies [79]. Another hypothesis is that B segregation can ease the mobility of GB dislocations and lower the local stress concentration and tendency for intergranular cracking [80].

An interesting issue that needs to be addressed here is that B can typically combine with Mo or Cr and form borides [46,81]. However, no boride precipitates were observed at the GBs or in the grain matrix of M2 alloys. This can be attributed due to the relatively low B content, low aging temperatures (732 °C and 621 °C), and slow cooling rate (air cooling) in this study, which control the equilibrium segregation of B at the GBs [82]. Such process conditions are unfavorable for the formation of borides, which generally require heat treatment temperatures above 850 °C [76,81,83]. In this case, B is prone to segregation into GBs, and the driving force for segregation is the reduction of the interfacial interaction energy, as formalized in terms of the classical Gibbs adsorption isotherm [84,85]. Owing to the occupation of B at the GBs, the nucleation of the F phase was retarded. In this regard, the ductility of the M2 sample was improved (Fig. 6), and the embrittling potency of hydrogen was largely reduced. It needs to clarify that, a ductility reduction of M2 sample was still observed in the hydrogen environment, which can be attributed to the fracture at dislocation slip bands and possible carbides in the matrix, as typically observed for nickel alloys. However, because the contribution from F phase-assisted hydrogen-induced cracking was eliminated, the GB embrittlement was removed and hydrogen resistant of M2 sample was largely improved. It also needs to mention that compared to M1 sample, 2.1 wt.% of Cu was

added to the M2 sample. However, STEM−EDS mapping shows no distribution inhomogeneity of Cu both in the matrix and at grain boundary. No precipitate containing Cu was observed, which indicates that Cu only participates in the solid solution effect [86].

5. Conclusions

To gain a deeper understanding of the failure mechanism of subsea nickel alloys, a thorough study on the hydrogen-induced degradation of nickel Alloy 725 was conducted by combining tensile tests, advanced characterization techniques and density functional theory (DFT) calculations. The results highlight the importance of the F phase for the onset of intergranular fracture of Alloy 725, in particular, under hydrogen occlusion. The transmission electron spectroscopy (TEM) results indicate that the F phase prefers to nucleate on the plane where $(111)_\gamma$ is parallel to the grain boundary (GB). In addition, atom probe tomography revealed the tortuosity of F-phase-decorated GBs. As corroborated by the DFT calculations, the interfacial interaction energy at the F phase/matrix interface could be substantially reduced in a hydrogen environment. Hydrogen thermal fluctuations and hydrogen-dislocation interactions at locations with high dislocation densities, such as dislocations piling up at interfaces and GBs, cause hydrogen concentration high enough to initiate cracks, which can be a critical reason for the intergranular fracture. These findings uncover the failure mechanisms of Alloy 725 by conforming to the hydrogen-enhanced decohesion and "Defactant" theories. As another highlight, the precise control of B addition could be an effective mitigation approach to eliminating the formation of the deleterious F phase. In general, this study conveys important information to the hydrogen embrittlement community in terms of both the fundamental understanding of hydrogen-induced failure mechanisms and the design of hydrogen-resistant nickel alloys. This shows that GB segregation engineering by modifying the alloying elements is a promising approach for designing hydrogen-resistant alloys by suppressing the nucleation of deleterious secondary phases.

CRediT authorship contribution statement

Xu Lu: Conceptualization, Methodology, Investigation, Data curation, Visualization, Writing – original draft. **Yan Ma**: Investigation, Writing – review & editing. **Yuan Ma**: Investigation, Data curation, Visualization, Writing – review & editing. **Dong Wang**: Investigation, Writing – review & editing. **Lei Gao**: Resources. **Wenwen Song**: Resources, Writing – review & editing. **Lijie Qiao**: Resources. **Roy Johnsen**: Supervision, Funding acquisition, Writing – review & editing.

Declaration of Competing Interest

The authors declare that they have no known competing financial interests or personal relationships that could have appeared to influence the work reported in this paper.

Data availability

The data that has been used is confidential.

Acknowledgements

X. Lu acknowledges Voestalpine Böhler Edelstahl GmbH & Co KG for providing laboratory-scale Alloy 725 samples. X. Lu and D. Wang acknowledge the financial support from the Research Council of Norway through the projects MHEAT (294689), HyLINE (294739), HYGROGENi (333118), Helife (344297) and the industry companies in the projects. The Research Council of Norway is acknowledged for the support to the Norwegian Micro- and Nano-Fabrication Facility, NorFab, project number 295864. X. Lu acknowledges Dr. Shuang He for the discussion and input on hydrogen trap occupancy analysis.

References

[1] R.B. Bhavsar, A. Collins, S. Silverman, Use of alloy 718 and 725 in oil and gas industry, Superalloys 718, 706 Var. Deriv. 625 (2001) 47–55.
[2] R. Krakow, D.N. Johnstone, A.S. Eggeman, D. Hunert, M.C. Hardy, C.M.F. Rae, P. A. Midgley, On the crystallography and composition of topologically close-packed phases in ATI 718Plus (R), Acta Mater. 130 (2017) 271–280.
[3] L.F. Liu, K. Tanaka, A. Hirose, K.F. Kobayashi, Effects of precipitation phases on the hydrogen embrittlement sensitivity of Inconel 718, Sci. Technol. Adv. Mat. 3 (4) (2002) 335–344.
[4] N. Totsuka, E. Lunarska, G. Cragnolino, Z. Szklarskasmialowska, Effect of hydrogen on the intergranular stress-corrosion cracking of Alloy-600 in high-temperature aqueous environments, Corrosion 43 (8) (1987) 505–514.
[5] V. Demetriou, J.D. Robson, M. Preuss, R. Morana, Study of the effect of hydrogen charging on the tensile properties and microstructure of four variant heat treatments of nickel alloy 718, Int J. Hydrog. Energ. 42 (37) (2017) 23856–23870.
[6] Z.B. Zhang, K.L. Moore, G. McMahon, R. Morana, M. Preuss, On the role of precipitates in hydrogen trapping and hydrogen embrittlement of a nickel-based superalloy, Corros. Sci. 146 (2019) 58–69.
[7] R.P. Gangloff, B.P. Somerday, Introduction, in: R.P. Gangloff, B.P. Somerday (Eds.), Gaseous Hydrogen Embrittlement of Materials in Energy Technologies, Woodhead Publishing, 2012, pp. xv–xix.
[8] R.J. Walter, R.P. Jewett, W.T. Chandler, On the mechanism of hydrogen-environment embrittlement of iron- and nickel-base alloys, Mater. Sci. Eng. 5 (2) (1970) 99–110.
[9] Z.B. Zhang, G. Obasi, R. Morana, M. Preuss, Hydrogen assisted crack initiation and propagation in a nickel-based superalloy, Acta Mater. 113 (2016) 272–283.
[10] Z. Tarzimoghadam, D. Ponge, J. Klöwer, D. Raabe, Hydrogen-assisted failure in Ni-based superalloy 718 studied under in situ hydrogen charging: The role of localized deformation in crack propagation, Acta Mater. 128 (2017) 365–374.
[11] X. Lu, D. Wang, D. Wan, Z.B. Zhang, N. Kheradmand, A. Barnoush, Effect of electrochemical charging on the hydrogen embrittlement susceptibility of alloy 718, Acta Mater. 179 (2019) 36–48.
[12] S. Jothi, S.V. Merzlikin, T.N. Croft, J. Andersson, S.G.R. Brown, An investigation of micro-mechanisms in hydrogen induced cracking in nickel-based superalloy 718, J. Alloy Compd. 664 (2016) 664–681.
[13] H. Andersson, C. Persson, In-situ SEM study of fatigue crack growth behaviour in IN718, Int. J. Fatigue 26 (3) (2004) 211–219.
[14] M. Seita, J.P. Hanson, S. Gradecak, M.J. Demkowicz, The dual role of coherent twin boundaries in hydrogen embrittlement, Nat. Commun. 6 (2015).
[15] J.P. Hanson, A. Bagri, J. Lind, P. Kenesei, R.M. Suter, S. Gradecak, M. J. Demkowicz, Crystallographic character of grain boundaries resistant to hydrogen-assisted fracture in Ni-base alloy 725, Nat. Commun. 9 (2018).
[16] Z.D. Harris, S.K. Lawrence, D.L. Medlin, G. Guetard, J.T. Burns, B.P. Somerday, Elucidating the contribution of mobile hydrogen-deformation interactions to hydrogen-induced intergranular cracking in polycrystalline nickel, Acta Mater. 158 (2018) 180–192.
[17] D. Di Stefano, M. Mrovec, C. Elsasser, First-principles investigation of hydrogen trapping and diffusion at grain boundaries in nickel, Acta Mater. 98 (2015) 306–312.
[18] S. He, W. Ecker, R. Pippan, V.I. Razumovskiy, Hydrogen- enhanced decohesion mechanism of the special Sigma 5(012)[100] grain boundary in Ni with Mo and C solutes, Comp, Mater. Sci. 167 (2019) 100–110.
[19] L.F. Liu, C. Lu, W.J. Ding, A. Hirose, K.F. Kobayashi, Effect of δ phase on hydrogen embrittlement of Inconel 718 by notch tensile tests, J. Mater. Sci. Technol. 21 (02) (2005) 256–260.
[20] R. Kirchheim, Reducing grain boundary, dislocation line and vacancy formation energies by solute segregation. I. Theoretical background, Acta Mater. 55 (15) (2007) 5129–5138.
[21] R. Kirchheim, Reducing grain boundary, dislocation line and vacancy formation energies by solute segregation II. Experimental evidence and consequences, Acta Mater. 55 (15) (2007) 5139–5148.
[22] R. Kirchheim, On the solute-defect interaction in the framework of a defactant concept, Int J. Mater. Res 100 (4) (2009) 483–487.
[23] F. Galliano, E. Andrieu, C. Blanc, J.-M. Cloue, D. Connetable, G. Odemer, Effect of trapping and temperature on the hydrogen embrittlement susceptibility of alloy 718, Mater. Sci. Eng.: A 611 (2014) 370–382.
[24] Y.F. Jiang, B. Zhang, Y. Zhou, J.Q. Wang, E.H. Han, W. Ke, Atom probe tomographic observation of hydrogen trapping at carbides/ferrite interfaces for a high strength steel, J. Mater. Sci. Technol. 34 (8) (2018) 1344–1348.
[25] X. Lu, Y. Ma, D. Wang, On the hydrogen embrittlement behavior of nickel-based alloys: Alloys 718 and 725, Mater. Sci. Eng. A 792 (2020).
[26] D.X. Li, K.H. Kuo, Some New Sigma-Related Structures Determined by High-Resolution Electron-Microscopy, Acta Crystallogr B 42 (1986) 152–159.
[27] Y.P. Lin, J.W. Steeds, Identification of a Hitherto Unreported Frank-Kasper Phase, Acta Crystallogr B 42 (1986) 159–162.
[28] M.S. Hazarabedian, M.Z. Quadir, M. Iannuzzi, Characterization of intergranular phases in precipitation hardening Ni alloy UNS N07725, Mater. Charact. 171 (2021).
[29] S. Mannan, F. Veltry, Time-temperature-transformation diagram of alloy 725, Superalloys 718, 706 Var. Deriv. 625 (2001) 345–356.
[30] A. Bhowmik, H.J. Stone, Microstructure and Mechanical Properties of Two-Phase Cr-Cr2Ta Alloys, Met. Mater. Trans. A 43a (9) (2012) 3283–3292.
[31] X. Lu, D. Wang, R. Johnsen, Hydrogen diffusion and trapping in nickel-based Alloy 625: an electrochemical permeation study, Electrochim. Acta (2022), 140477.

[32] J. Xu, X.K. Sun, Q.Q. Liu, W.X. Chen, Hydrogen permeation behavior in In718 and Gh761 superalloys, Met. Mater. Trans. A 25 (3) (1994) 539–544.
[33] J. Crank. The Mathematics of Diffusion, 2nd ed..,, Clarendon,, Oxford, 1975.
[34] W. Kohn, L.J. Sham, Self-consistent equations including exchange and correlation effects, Phys. Rev. 140 (4A) (1965) A1133–A1138.
[35] G. Kresse, J. Furthmüller, Efficient iterative schemes for ab initio total-energy calculations using a plane-wave basis set, Phys. Rev. B 54 (16) (1996) 11169–11186.
[36] J.P. Perdew, K. Burke, M. Ernzerhof, Generalized gradient approximation made simple, Phys. Rev. Lett. 77 (18) (1996) 3865–3868.
[37] P.E. Blochl, Projector Augmented-Wave Method, Phys. Rev. B 50 (24) (1994) 17953–17979.
[38] L.E. Shoemaker, Alloys 625 and 725: Trends in properties and applications, Superalloys 718, 625, 706 and Derivatives, Proceedings (2005) 409–418.
[39] Y. Chen, X. Liu, T. Zhang, H. Xie, N. Zhao, C. Shi, C. He, J. Li, E. Liu, Interface intrinsic strengthening mechanism on the tensile properties of Al2O3/Al composites, Comp, Mater. Sci. 169 (2019), 109131.
[40] G. Di Liberto, Á. Morales-García, S.T. Bromley, An unconstrained approach to systematic structural and energetic screening of materials interfaces, Nat. Commun. 13 (1) (2022) 6236.
[41] X. Pang, J. Yang, M. Pang, J. He, W. Yang, H. Qin, Y. Zhan, Theoretical understanding of atomic and electronic structures of the ZrC(111)/Cu(111,) Interface, J. Alloy Compd. 791 (2019) 431–437.
[42] K. Zhang, Y. Abbas, S.U. Jan, L. Gao, Y. Ma, Z. Mi, X. Liu, Y. Xuan, J.R. Gong, Selective Growth of Stacking Fault Free ⟨100⟩ Nanowires on a Polycrystalline Substrate for Energy Conversion Application, ACS Appl. Mater. Interfaces 12 (15) (2020) 17676–17685.
[43] A.S. Wilson, Formation and effect of topologically close-packed phases in nickel-base superalloys, Mater. Sci. Tech. -Lond. 33 (9) (2017) 1108–1118.
[44] B. Seiser, R. Drautz, D.G. Pettifor, TCP phase predictions in Ni-based superalloys: Structure maps revisited, Acta Mater. 59 (2) (2011) 749–763.
[45] Hu Rehman, K. Durst, S. Neumeier, A.B. Parsa, A. Kostka, G. Eggeler, M. Göken, Nanoindentation studies of the mechanical properties of the μ phase in a creep deformed Re containing nickel-based superalloy, Mater. Sci. Eng.: A 634 (2015) 202–208.
[46] P. Kontis, A. Kostka, D. Raabe, B. Gault, Influence of composition and precipitation evolution on damage at grain boundaries in a crept polycrystalline Ni-based superalloy, Acta Mater. 166 (2019) 158–167.
[47] P. Kontis, E. Alabort, D. Barba, D.M. Collins, A.J. Wilkinson, R.C. Reed, On the role of boron on improving ductility in a new polycrystalline superalloy, Acta Mater. 124 (2017) 489–500.
[48] R.L. Morrison, S.J. Fensin, J.L.W. Carter, Exploration of the sliding behavior of a Sigma 11 grain boundary with precipitates in Ni-Al system using molecular dynamics, Materialia 7 (2019).
[49] F.G. Wei, K. Tsuzaki, Quantitative analysis on hydrogen trapping of TiC particles in steel, Met. Mater. Trans. A 37a (2) (2006) 331–353.
[50] Y. Ma, Y.F. Shi, H.Y. Wang, Z.S. Mi, Z.G. Liu, L. Gao, Y. Yan, Y.J. Su, L.J. Qiao, A first-principles study on the hydrogen trap characteristics of coherent nano-precipitates in alpha-Fe, Int J. Hydrog. Energ. 45 (51) (2020) 27941–27949.
[51] D. McLean, Grain Boundaries in Metals, Clarendon Press,, Oxford, 1957.
[52] R.A. Oriani, The diffusion and trapping of hydrogen in steel, Acta Metall. 18 (1) (1970) 147–157.
[53] K. Wada, J. Yamabe, H. Matsunaga, Visualization of trapped hydrogen along grain boundaries and its quantitative contribution to hydrogen-induced intergranular fracture in pure nickel, Materialia 8 (2019), 100478.
[54] J.E. Angelo, N.R. Moody, M.I. Baskes, Trapping of hydrogen to lattice-defects in nickel, Model Simul. Mater. Sc. 3 (3) (1995) 289–307.
[55] W.T. Geng, A.J. Freeman, R. Wu, C.B. Geller, J.E. Raynolds, Embrittling and strengthening effects of hydrogen, boron, and phosphorus on a Sigma 5 nickel grain boundary, Phys. Rev. B 60 (10) (1999) 7149–7155.
[56] M. Yamaguchi, M. Shiga, H. Kaburaki, Energetics of segregation and embrittling potency for non-transition elements in the Ni Sigma 5 (012) symmetrical tilt grain boundary: a first-principles study, J. Phys. -Condens Mat. 16 (23) (2004) 3933–3956.
[57] M. Yamaguchi, M. Shiga, H. Kaburaki, First-principles study on segregation energy and embrittling potency of hydrogen in Ni Sigma 5(012) tilt grain boundary, J. Phys. Soc. Jpn 73 (2) (2004) 441–449.
[58] J.G.A. Young, R. Najafabadi, W. Strohmayer, D.G. Baldrey, B. Hamm, J. Harris, J. Sticht, E. Wimmer, An Atomistic Modeling Study of Alloying Element Impurity Element, and Transmutation Products on the cohesion of A Nickel E5 {l_brace}001 {r_brace} Twist Grain Boundary, United States, 2003.
[59] A. Turnbull, R.G. Ballinger, I.S. Hwang, M.M. Morra, M. Psailadombrowski, R. M. Gates, Hydrogen Transport in Nickel-Base Alloys, Met. Trans. A 23 (12) (1992) 3231–3244.
[60] N.R. Moody, S.L. Robinson, S.M. Myers, F.A. Greulich, Deuterium Concentration Profiles in Fe-Ni-Co Alloys Electrochemically Charged at Room-Temperature, Acta Metall. 37 (1) (1989) 281–290.
[61] D.M. Symons, G.A. Young, J.R. Scully, The effect of strain on the trapping of hydrogen at grain-boundary carbides in Ni-Cr-Fe alloys, Met. Mater. Trans. A 32 (2) (2001) 369–377.
[62] R. Silverstein, D. Eliezer, E. Tal-Gutelmacher, Hydrogen trapping in alloys studied by thermal desorption spectrometry, J. Alloy. Compd. 747 (2018) 511–522.
[63] Y.-S. Chen, H. Lu, J. Liang, A. Rosenthal, H. Liu, G. Sneddon, I. McCarroll, Z. Zhao, W. Li, A. Guo, J.M. Cairney, Observation of hydrogen trapping at dislocations, grain boundaries, and precipitates, Science 367 (6474) (2020) 171–175.
[64] B. Zhang, Q. Zhu, C. Xu, C. Li, Y. Ma, Z. Ma, S. Liu, R. Shao, Y. Xu, B. Jiang, L. Gao, X. Pang, Y. He, G. Chen, L. Qiao, Atomic-scale insights on hydrogen trapping and exclusion at incoherent interfaces of nanoprecipitates in martensitic steels, Nat. Commun. 13 (1) (2022) 3858.
[65] Y. Ogawa, K. Noguchi, O. Takakuwa, Criteria for hydrogen-assisted crack initiation in Ni-based superalloy 718, Acta Mater. 229 (2022), 117789.
[66] C.J. McMahon, Hydrogen-induced intergranular fracture of steels, Eng. Fract. Mech. 68 (6) (2001) 773–788.
[67] W.W. Gerberich, Modeling hydrogen induced damage mechanisms in metals, Gaseous Hydrog. Embrittlement Mater. Energy Technol. 2 (2012) 209–246.
[68] W.W. Gerberich, R.A. Oriani, M.J. Lii, X. Chen, T. Foecke, The necessity of both plasticity and brittleness in the fracture thresholds of iron, Philos. Mag. A: Phys. Condens. Matter.: Defects Mech. Prop. 63 (2) (1991) 363–376.
[69] R. Kirchheim, Revisiting hydrogen embrittlement models and hydrogen-induced homogeneous nucleation of dislocations, Scr. Mater. 62 (2) (2010) 67–70.
[70] K. Takai, H. Shoda, H. Suzuki, M. Nagumo, Lattice defects dominating hydrogen-related failure of metals, Acta Mater. 56 (18) (2008) 5158–5167.
[71] T. Hu, S. Yang, N. Zhou, Y. Zhang, J. Luo, Role of disordered bipolar complexions on the sulfur embrittlement of nickel general grain boundaries, Nat. Commun. 9 (1) (2018) 2764.
[72] M.S. Hazarabedian, N. Haghdadi, S. Primig, M. Lison-Pick, M.Z. Quadir, M. Ferry, M. Iannuzzi, Formation of intergranular phases in precipitation hardening nickel-based alloy 725, Acta Mater. 236 (2022), 118108.
[73] D. Tytko, P.P. Choi, J. Klower, A. Kostka, G. Inden, D. Raabe, Microstructural evolution of a Ni-based superalloy (617B) at 700 degrees C studied by electron microscopy and atom probe tomography, Acta Mater. 60 (4) (2012) 1731–1740.
[74] M. Yamaguchi, First-Principles Study on the Grain Boundary Embrittlement of Metals by Solute Segregation: Part I. Iron (Fe)-Solute (B, C, P, and S) Systems, Met. Mater. Trans. A 42a (2) (2011) 319–329.
[75] C.L. Briant, R.P. Messmer, An Electronic Model for the Effect of Alloying Elements on the Phosphorus Induced Grain-Boundary Embrittlement of Steel, Acta Metall. 30 (9) (1982) 1811–1818.
[76] S.H. Song, T.D. Xu, Z.X. Yuan, Z.S. Yu, Equilibrium Grain-Boundary Segregation and the Effect of Boron in B-Doped Fe-30 wtPercent Ni Austenitic Alloy, Acta Met. Mater. 39 (5) (1991) 909–914.
[77] U. Franzoni, F. Marchetti, S. Sturlese, Effects of Grain-Boundary Segregation and Precipitation on the Creep-Behavior of a 20cr, Al-Ti, Ni-Base Superalloy, Scr. Met. Mater. 19 (4) (1985) 511–516.
[78] A.S. Ebner, S. Jakob, H. Clemens, R. Pippan, V. Maier-Kiener, S. He, W. Ecker, D. Scheiber, V.I. Razumovskiy, Grain boundary segregation in Ni-base alloys: A combined atom probe tomography and first principles study, Acta Mater. 221 (2021).
[79] T.J. Garosshen, T.D. Tillman, G.P. Mccarthy, Effects of B, C, and Zr on the Structure and Properties of a P/M Nickel-Base Superalloy, Met. Trans. A 18 (1) (1987) 69–77.
[80] E.M. Schulson, T.P. Weihs, I. Baker, H.J. Frost, J.A. Horton, Grain boundary accommodation of slip in Ni3Al containing boron, Acta Metall. 34 (7) (1986) 1395–1399.
[81] P. Kontis, H.A.M. Yusof, S. Pedrazzini, M. Danaie, K.L. Moore, P.A.J. Bagot, M. P. Moody, C.R.M. Grovenor, R.C. Reed, On the effect of boron on grain boundary character in a new polycrystalline superalloy, Acta Mater. 103 (2016) 688–699.
[82] G. Da Rosa, P. Maugis, A. Portavoce, J. Drillet, N. Valle, E. Lentzen, K. Hoummada, Grain-boundary segregation of boron in high-strength steel studied by nano-SIMS and atom probe tomography, Acta Mater. 182 (2020) 226–234.
[83] W. Chen, M.C. Chaturvedi, N.L. Richards, G. McMahon, Grain boundary segregation of boron in INCONEL 718, Metall. Mater. Trans. A: Phys. Metall. Mater. Sci. 29 (7) (1998) 1947–1954.
[84] D. Raabe, M. Herbig, S. Sandlöbes, Y. Li, D. Tytko, M. Kuzmina, D. Ponge, P. P. Choi, Grain boundary segregation engineering in metallic alloys: A pathway to the design of interfaces, Curr. Opin. Solid State Mater. Sci. 18 (4) (2014) 253–261.
[85] H.J. Grabke, Surface and grain boundary segregation on and in iron and steels, ISIJ Int. 29 (7) (1989) 529–538.
[86] I. Taji, T. Hajilou, A.S. Ebner, D. Scheiber, S. Karimi, E. Plesiutschnig, W. Ecker, A. Barnoush, V. Maier-Kiener, R. Johnsen, V.I. Razumovskiy, Hydrogen assisted intergranular cracking of alloy 725: The effect of boron and copper alloying, Corros. Sci. 203 (2022), 110331.